

An air-breathing microfluidic formic acid fuel cell with a porous planar anode: experimental and numerical investigations

This article has been downloaded from IOPscience. Please scroll down to see the full text article.

2010 J. Micromech. Microeng. 20 105008

(<http://iopscience.iop.org/0960-1317/20/10/105008>)

View [the table of contents for this issue](#), or go to the [journal homepage](#) for more

Download details:

IP Address: 155.69.4.4

The article was downloaded on 05/09/2010 at 16:19

Please note that [terms and conditions apply](#).

An air-breathing microfluidic formic acid fuel cell with a porous planar anode: experimental and numerical investigations

Seyed Ali Mousavi Shaegh, Nam-Trung Nguyen and Siew Hwa Chan

School of Mechanical and Aerospace Engineering, Nanyang Technological University,
50 Nanyang Avenue, Singapore 639798

E-mail: mntnguyen@ntu.edu.sg

Received 19 June 2010

Published 3 September 2010

Online at stacks.iop.org/JMM/20/105008

Abstract

This paper reports the fabrication, characterization and numerical simulation of an air-breathing membraneless laminar flow-based fuel cell with carbon-fiber-based paper as an anode. The fuel cell uses 1 M formic acid as the fuel. Parameters from experimental results were used to establish a three-dimensional numerical model with COMSOL Multiphysics. The simulation predicts the mass transport and electrochemical reactions of the tested fuel cell using the same geometry and operating conditions. Simulation results predict that the oxygen concentration over an air-breathing cathode is almost constant for different flow rates of the fuel and electrolyte. In contrast, the growth of a depletion boundary layer of the fuel over the anode can be the major reason for low current density and low fuel utilization. At a low flow rate of $10 \mu\text{l min}^{-1}$, simulation results show a severe fuel diffusion to the cathode side, which is the main reason for the degradation of the open-circuit potential from 0.78 V at $500 \mu\text{l min}^{-1}$ to 0.58 V at $10 \mu\text{l min}^{-1}$ as observed in experiments. Decreasing the total flow rate 50 times from $500 \mu\text{l min}^{-1}$ to $10 \mu\text{l min}^{-1}$ only reduces the maximum power density approximately two times from 7.9 to 3.9 mW cm^{-2} , while fuel utilization increases from 1.03% to 38.9% indicating a higher fuel utilization at low flow rates. Numerical simulation can be used for further optimization, to find a compromise between power density and fuel utilization.

(Some figures in this article are in colour only in the electronic version)

1. Introduction

A membraneless laminar flow-based fuel cell (LFFC) is an emerging category of micro fuel cells [1]. This fuel cell concept utilizes the effect of stable liquid interface in co-laminar flows at microscale. Since a LFFC uses a liquid–liquid interface to separate the fuel and oxidant, some membrane-related problems such as flooding and dry-out are eliminated. A proper selection of the flow channel design and flow rate is required to avoid issues related to the dynamic liquid–liquid interface such as diffusion mixing of the reactive streams.

Low oxygen solubility in aqueous media is a major reason for the low performance of LFFCs [2]. To address this issue, some solutions were utilized with high concentration and high solubility of oxidants such as hydrogen peroxide [3] or vanadium redox couples [4]. Air-breathing capability

would allow the practical use of micro fuel cells and their entry into the commercial market. The air-breathing LFFC with an integrated air-breathing gas diffusion cathode [5–7] would further simplify the device design and avoid the need for an external reservoir for the oxidant solution. These LFFCs benefit from the high concentration of oxygen in air of 10 mM and the higher diffusion coefficient of oxygen in air of $0.2 \text{ cm}^2 \text{ s}^{-1}$ compared to the respective values in aqueous media of 2–4 mM and $2 \times 10^{-5} \text{ cm}^2 \text{ s}^{-1}$ [5].

In the air-breathing LFFC, instead of an oxidant stream a stream of electrolyte is used to form the fuel–electrolyte interface and to separate the fuel stream from the cathode side, figure 1. On one hand, diffusive mixing between the fuel and the electrolyte reduces the fuel utilization in a single pass and degrades the performance due to the lower concentration of the fuel in the vicinity of the anode. On the other

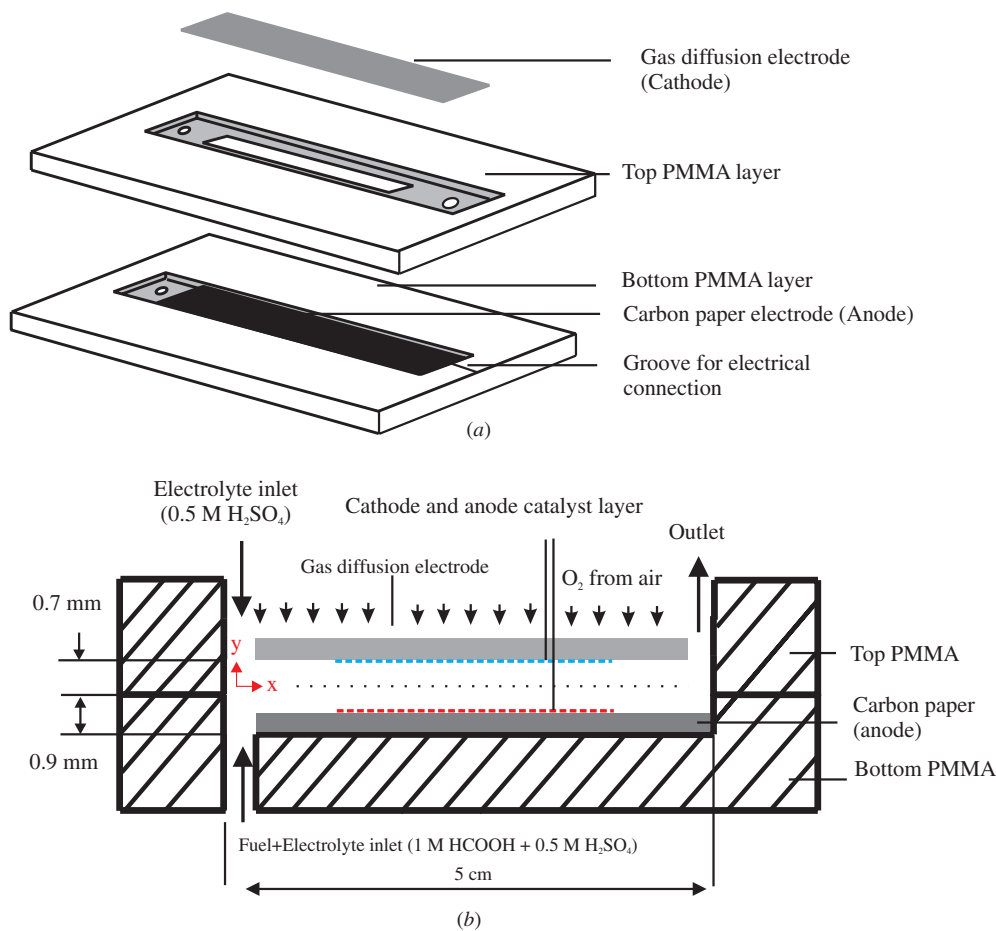


Figure 1. Schematic of the microfluidic fuel cell: (a) the different layers; (b) details of fuel cell architecture (not to scale).

hand, diffusive mixing leads to fuel crossover and mixed potential at the cathode. Therefore, controlling the dynamic fuel–electrolyte interface is a major design consideration and the main objective for the optimization of a LFFC.

In order to decrease fuel crossover, Hollinger *et al* [8] implemented a thin nanoporous separator (polycarbonate with $0.05\ \mu\text{m}$ pore size and a pore density of $6 \times 10^8\ \text{pores cm}^{-2}$) at the fuel–electrolyte interface which reduces the liquid–liquid contact between the two streams by 98.8%. Applying this method and using a thin layer of Nafion over the cathode to decrease the fuel diffusion to the catalyst layer, the peak power density is increased by a factor of 2.5 from 28 to $40\ \text{mW cm}^{-2}$ at $80\ ^\circ\text{C}$ running by methanol.

Tominaka *et al* [9] reported a micro direct methanol fuel cell with an integrated air-breathing cathode. The whole cell, which is a channel with an open top, was fabricated in silicon as a monolithic structure that omits the electrolyte stream to separate the fuel stream from the cathode. Palladium–cobalt (Pd–Co) alloy electro-deposited on a thin layer of gold works as the current collector. With sulfuric acid (H_2SO_4) as the supportive electrolyte, the open-circuit voltage and the maximum power reach $0.5\ \text{V}$ and $1.4\ \mu\text{W}$, respectively.

One strategy for further miniaturization and to achieve a more practical design for commercialization is the elimination of the electrolyte stream. Whipple *et al* [7] developed a fuel-tolerant catalyst for the oxygen electro-reduction

reactions using ruthenium–selenium chalcogenides (Ru_xSe_y). However, the absolute performance of the cell with (Ru_xSe_y) is lower than the cell with a platinum (Pt) cathode by a factor of 4 ($4\ \text{mW cm}^{-2}$ versus $16\ \text{mW cm}^{-2}$). But with this concept, methanol crossover is not a concern anymore, and the electrolyte can be eliminated as the separating stream. Also, a much higher fuel concentration can be used so that the energy density of the cell can be improved.

To consider different strategies and design considerations for the performance optimization, a quantitative determination of species concentration distribution within the fuel cell is inevitable. Some works on modeling and numerical simulation have been carried out to provide a better understanding of electrochemical reactions and mass transport in conventional LFFCs with the aqueous fuel and oxidant streams in a microchannel [11–15]. In a recent study, Jayashree *et al* [10] predicted the concentration of formic acid in the microchannel of an air-breathing LFFC for a cell potential of $0.3\ \text{V}$. Their simulation was based on a three-dimensional (3D) finite-element-method (FEM) model implemented in Femlab 3.2 from COMSOL. Diffusive mixing and fuel utilization for the fuel-to-electrolyte rate ratios of 1:1 and 1:5 were investigated.

In the current study, an air-breathing LFFC with a porous anode was fabricated and characterized experimentally for three different flow rates. A 3D model was established in COMSOL in order to solve the species transport equations with

corresponding electrochemical reactions over the anode and the air-breathing cathode. This model provides quantitative explanation for the performance of the fuel cell at different flow rates and different operating conditions. Also, in order to determine the contribution of different polarization losses in the current–voltage polarization curve, anodic and cathodic activation polarization losses were calculated and discussed. Good quantitative agreement between the experimental and numerical results in terms of the predicted current–voltage curve and fuel utilization indicates that the model can be used as a platform to investigate different flow architectures in various operating conditions for the optimization of the fuel cell.

2. Fabrication of the fuel cell

Figure 1 depicts the schematic of our air-breathing LFFC. The fuel cell is mainly made of two pieces of PMMA which were machined by a CO₂ laser. The bottom layer is a 2 mm thick PMMA sheet with engraved micro channel for the fuel stream. The channel width and length are 2 mm and 5 cm, respectively. The channel height of 0.9 mm was engraved in the PMMA sheet by precisely adjusting the laser power and scanning speed of the laser machining system (Universal M-300 Laser Platform, Universal Laser Systems Inc., AZ, USA). A piece of plain Toray carbon paper with a typical thickness of 280 μm , a porosity of approximately 78% [18], a width of 2 mm and a length of 4 cm was placed at the bottom of the channel to work as the anode. The final active area of the anode measures 2 mm \times 30 mm. The active area was coated with platinum–ruthenium (Pt–Ru) alloy nanoparticles working as an electrocatalyst. It is to be noted that the electro-oxidation of formic acid on Pt and selected Pt-group metal surfaces is a dual pathway mechanism. Adsorbed carbonate monoxide can be produced at the formic acid dehydration pathway which is a poisoning intermediate and can block the dehydrogenation pathway, which is the direct path for generating an active intermediate of H⁺ and releasing electrons [16, 17]. Since utilization of Pt–Ru can increase the rate of formic acid electro-oxidation [16], catalyst ink was prepared using 10 mg cm^{−2} of Pt–Ru 20:20 atom wt% alloy (E-TEK) and 1.5 mg cm^{−2} of Nafion (5 wt% Nafion 5112, DuPont). After extensive ultrasound mixing, the ink was spread on the top surface of the anode to produce the 0.6 cm² active area for formic acid oxidation.

A 1 mm thick PMMA sheet was cut by the same CO₂ laser system to work as the cover for the channel. This PMMA layer has a 2 mm \times 30 mm slot to hold the cathode made of Toray carbon paper. The carbon paper was dipped in a 5% polytetrafluoroethylene (PTFE) solution for 2 min. After drying at room temperature, the paper was baked at 250 °C for 30 min and at 350 °C for another 30 min to prepare a hydrophobic surface. The PTFE coating avoids liquid leakage from the channel through the porous carbon paper to the environment. It is noteworthy that the immersion of the carbon paper in the PTFE solution decreases its porosity depending on the content of the PTFE solution [18]. For 5% PTFE content, the porosity decrease is less than 1% [18].

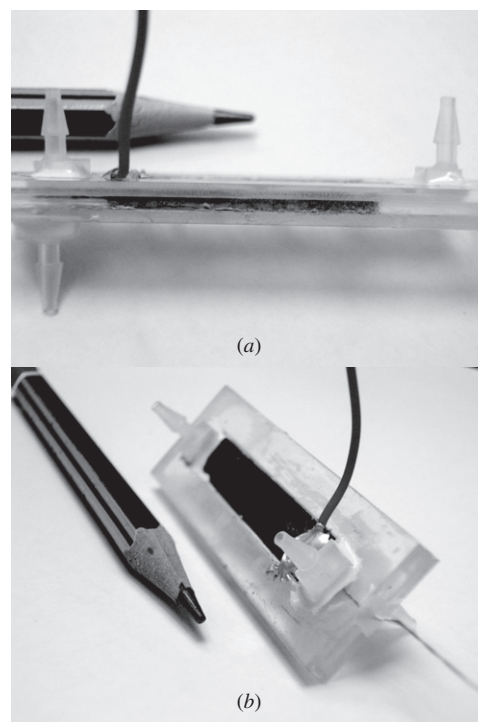


Figure 2. Fabricated fuel cell: (a) arrangement of inlets and outlet; (b) GDE and wires attached to the anode and cathode.

The cathode has a double-layer catalyst loading [6]. The first layer contains 0.3 mg cm^{−2} platinum nanoparticles supported on Vulcan XC 72 (Alfa-Aesar). The second layer, which is exposed directly to the liquid electrolyte (0.5 M sulfuric acid), has a loading of 2 mg cm^{−2} platinum and approximately 0.1 mg cm^{−2} of Nafion to enhance the proton conductivity. The gas diffusion electrode (GDE) is assembled on the PMMA sheet using epoxy (Araldite, Huntsmann, USA). Before bonding the two PMMA sheets, both PMMA surfaces are mechanically treated by fine sand papers to improve the surface roughness for better adhesion. The two PMMA pieces were then bonded together using chloroform. Electrically conducting copper wires were attached to the electrodes using conductive silver epoxy (Chemtronics, USA). The electrodes are aligned and positioned to maintain the 0.6 cm² active surface area on both electrodes. The fuel and electrolyte inlets were cut by the laser system and have a diameter of 1.3 mm. A single outlet with a diameter of 2 mm was cut on the top layer. Fluidic interconnects were glued to the cell using epoxy adhesive. Tubing with an inner diameter of 0.062 inch and outer diameter of 0.125 inch (Cole–Parmer) was used for delivering the fuel, electrolyte and waste. After the final assembly, the LFFC was tested for leakage with de-ionized (DI) water. Figure 2 depicts the assembled LFFC.

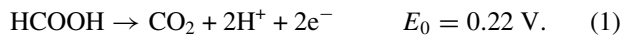
3. Characterization of the fuel cell

Our LFFC is running by a solution of 1 M formic acid with 0.5 M sulfuric acid (supportive electrolyte) as a fuel and a stream of 0.5 M sulfuric acid as an electrolyte. Formic acid, compared with methanol, has a faster kinetics of electro-oxidation at room temperature [20]. Also, formic acid is

a strong electrolyte, so it can enhance both electronic and proton transport at the anode side, and also it is common to the environment [21].

The electrolyte stream separates the fuel from direct exposure to the cathode. The flow rate of the fuel and that of the electrolyte streams are kept constant at a fixed ratio of 1:1. The fuel cell was tested with the fuel flow rates of 10, 100 and 500 $\mu\text{l min}^{-1}$. Both fuel and electrolyte streams were delivered by a syringe pump (KD Scientific). Introducing the electrolyte stream into the channel has two main functions. The first function is to avoid mixed potential due to the oxidation of formic acid at the cathode that can dramatically reduce the performance [7]. The second function is preventing the catalyst poisoning due to formic acid oxidation at the Pt-supported cathode. Both catalyst poisoning and mixed potential on the cathode are the consequences of fuel diffusion from the anode to cathode across the channel. Fuel diffusion can be minimized by the fine adjustment of fuel and electrolyte streams.

The generation of electricity in the LFFC follows the electrochemical reactions at the anode and cathode. At the anode, formic acid decomposes and creates electrons and protons:



Oxygen diffusing into the catalyst layer of the gas diffusion electrode reacts with electrons coming from the anode and protons travelling across the channel to form water. The catalytic oxygen reduction reaction (ORR) is a multi-electron process with a number of elementary steps, entailing different reaction intermediates [19]. Without considering the reaction intermediates, the oxygen reduction at the cathode is considered as



The characterization was carried out at room temperature of 25 °C. The current at different cell potentials was measured with an electric load system (Solartron Analytical, Solartron Group Limited, UK). The results were evaluated with the MultiStat electrochemistry software (Scribner Associates Inc., USA). Data were recorded after a stable condition of the flow rate is reached. Based on the dimension of the flow channel and the flow rates, the residence time of the fuel from the inlet to the outlet of the cell ranges approximately from 10 to 500 s. Thus, a potential scanning rate of 5 mV s⁻¹ can provide enough time to capture effects such as diffusive mixing at the interface of the laminar streams.

4. Modeling the transport and electrochemical phenomena

To have quantitative understanding of the experimental results, a three-dimensional model based on the FEM software (COMSOL Multiphysics) was established. The model solved the coupled electrochemical reactions and transport phenomena within the fuel cell at the same experimental operating conditions and the same geometry.

4.1. Hydrodynamic equations

To solve the flow field in the channel and through the porous anode, Navier–Stokes and continuity equations are solved for the steady-state, laminar flow ($Re < 10$). The isothermal condition inside the channel and negligible body forces are assumed:

$$\nabla \cdot (\rho \mathbf{u}) = 0 \quad (3)$$

$$\nabla \cdot (\mathbf{u}\mathbf{u}) = -\frac{1}{\rho} \nabla p + \nabla \cdot (\nu \nabla \mathbf{u}), \quad (4)$$

where p is the static pressure, \mathbf{u} is the velocity vector, ρ is the fluid density and ν is the kinematic viscosity. The system is considered as an isothermal system because the viscous dissipation due to the low liquid velocities through the channel ($u < 1 \text{ cm s}^{-1}$) can be neglected [11]. Since the anolyte and electrolyte are dilute solutions, the input density of the anolyte and electrolyte are considered as that of water.

To solve the flow distribution in the porous media, Darcy's law is used [22]:

$$\mathbf{u} = -\frac{k}{\mu} \nabla p, \quad (5)$$

where k is the intrinsic permeability of the porous media. Intrinsic permeability, which is known as the permeability for the single phase flow, is independent of the nature of the fluid and dependent on the geometry of the medium [22].

4.2. Mass transport and the electrochemical model

The electro-oxidation of formic acid to carbon dioxide CO_2 on a metal surface is accepted to take place via a dual path mechanism, dehydrogenation and dehydration [17]. In the current model, the direct pathway is assumed to be the dominant mechanism for the oxidation of formic acid as indicated in (1). The catalytic ORR is a multi-electron process with a number of elementary steps, entailing different reaction intermediates [19]. Without considering the reaction intermediates, the oxygen reduction at the cathode is considered as denoted by (2).

The electrochemical reaction takes place over electrodes. Both anode and cathode are made of porous carbon paper covered by a thin layer of catalyst particles. The catalyst layer is treated as a boundary, where the corresponding electrochemical reactions take place over these boundaries. So the effect of these reactions on the species concentration appears as the source term, S_i , in the equation of conservation of species:

$$\nabla \cdot (-D_i \nabla C_i + C_i \mathbf{u}) = S_i, \quad (6)$$

where S_i is the net rate of change of the species ' i ' by electrochemical reactions over the anode and cathode and represents the rate of consumed species per cubic meter. D_i is the diffusion coefficient of the species ' i ' in the corresponding media, which refers to formic acid in the anode and oxygen in the cathode. So the values of D for anodic and cathodic reactions are considered as formic acid diffusivity in aqueous media (water) and oxygen diffusivity through the GDE, which is made of carbon paper, and the aqueous media of electrolyte,

Table 1. The value of input constants for the simulation.

Parameter	Description	Values used	Units
$C_{0,\text{HCOOH}}$	Reference concentration of formic acid	500	mol m^{-3}
C_{0,O_2}	Reference concentration of oxygen	85	mol m^{-3}
$D_{\text{O}_2(\text{H}_2\text{O})}$	Diffusivity of oxygen in water	2.1×10^{-9}	$\text{m}^2 \text{s}^{-1}$
$D_{\text{O}_2(\text{air})}$	Diffusivity of oxygen in air	2.1×10^{-5}	$\text{m}^2 \text{s}^{-1}$
D_{HCOOH}	Diffusivity of formic acid as anolyte	2.546×10^{-9}	$\text{m}^2 \text{s}^{-1}$
n_a	Number of transferred electrons at the anode	2	–
n_c	Number of transferred electrons at the cathode	4	–
F	Faraday's constant	96 485	C mol^{-1}
$j_{0,a}$	Exchange current density at the anode	600	A m^{-2}
$j_{0,c}$	Exchange current density at the cathode	5×10^{-1}	A m^{-2}
k	In-plane permeability of carbon paper	1×10^{-12}	m^2
K	Electrical conductivity of electrodes	300	$(\Omega \text{ m})^{-1}$
R	Universal gas constant	8.314	$\text{J mol}^{-1} \text{K}^{-1}$
T	Temperature	298	K
α_a	Anodic charge transfer coefficient, anode and cathode	0.5	–
α_c	Cathodic charge transfer coefficient, anode and cathode	0.5	–
ε	Porosity of carbon paper used as a GDE and anode	0.7	–
μ	Viscosity	10^{-3}	$\text{kg m}^{-1} \text{s}^{-1}$
ρ	Density of anolyte and electrolyte stream	1000	kg m^{-3}
τ	Tortuosity of carbon paper	3	–

respectively. C is the concentration of the corresponding species in the anode and cathode.

The rate of formic acid electro-oxidation in the anode and the electro-reduction of oxygen in the cathode are given by

$$S_i = \left(\frac{j_0}{n_i F} \right) \left(\frac{C_i}{C_{i,\text{ref}}} \right)^{\beta_i} \left[\exp \left(\frac{\alpha_a F \eta}{RT} \right) - \exp \left(-\frac{\alpha_c F \eta}{RT} \right) \right], \quad (7)$$

where j_0 is the exchange current density at the reference reactant concentration $C_{i,\text{ref}}$ and β_i is the reaction order of the species ' i ' for the elementary charge transfer step. Since the rate determining step is a first-order reaction, $\beta = 1$ is chosen [11], α_a and α_c are the anodic and cathodic charge transfer coefficients, respectively, R is the universal constant, T is the operating temperature and considered as a constant parameter, F is the Faraday constant and η is the activation overpotential.

Oxygen from the atmosphere diffuses through the GDE to reach the catalyst layer. To determine the oxygen concentration through the GDE, equations (6) and (7) are solved with input values and appropriate boundary conditions listed in tables 1 and 2.

On the catalytic surface, only the normal flux to the surface contributes to the power output of the cell and is given by

$$\mathbf{n} \cdot \nabla \cdot (-D_{ij} \nabla C_i + C_i \mathbf{u}) = S_i. \quad (8)$$

Due to the porous structure of the cathode and anode, the binary diffusion coefficients utilized in the porous media are corrected for the porosity (ε) and tortuosity (τ) of the media as follows [23]:

$$D_{ij}^{\text{eff}} = D_{ij} \frac{\varepsilon}{\tau}. \quad (9)$$

In addition to proton diffusion to the cathode side, formic acid can diffuse and reach the cathode at low flow rates. Formic acid adjacent to the cathode catalyst can be oxidized decreasing the cathode voltage due to the mixed potential. In this model the effect of fuel crossover on the cathode is not considered.

Table 2. Boundary conditions used for hydrodynamic and electrochemical reactions, reproduced after [10].

Boundary conditions to solve equations (3) and (4)
$\mathbf{u} = (0, u_0)$, where u_0 is the inlet velocity (0.006, 0.0012, 0.000 12 m s^{-1})
$\mathbf{u} = (0, 0)$ at the walls
$p = 0$ at the outlet
Boundary conditions to solve equation (6) for anode and cathode reactions:
$C = C_0$ at the inlet of anolyte stream
$C = 0$ at the inlet of electrolyte stream
$(-D \nabla C + C \mathbf{u}) \cdot \mathbf{n} = 0$ at the non-catalytic walls
$(-D \nabla C) \cdot \mathbf{n} = 0$ at the outlet

4.3. Boundary conditions

The fuel-to-electrolyte flow rate ratio of 1:1 is chosen while the outlet hydrodynamic boundary condition is set on zero pressure. The software is run for three different flow rates, 500, 100 and 10 $\mu\text{l min}^{-1}$, which can be addressed as Q_1 , Q_2 and Q_3 with the corresponding inlet velocities of 0.006, 0.0012 and 0.00012 m s^{-1} , respectively.

To solve the mass transport, the constant concentration of formic acid (1 M) is set at the inlet for the anolyte stream for all simulations, while the concentration of formic acid at the inlet of the electrolyte stream is set to be zero. Also, the outlet condition is convective mass transport. For the GDE, the upper surface exposed to the ambient air has an inlet concentration equal to the oxygen concentration of the atmosphere ($0.21 p_{\text{atm}}/RT$) [24], while the bottom surface, working as a catalytic surface, has an inward flux of S_{O_2} from equation (7). At the liquid–liquid interface between two streams, the continuity condition was applied for velocity and species concentration. All used parameters to solve the required equations are listed in tables 1 and 2, where the values are compiled from [23–27].

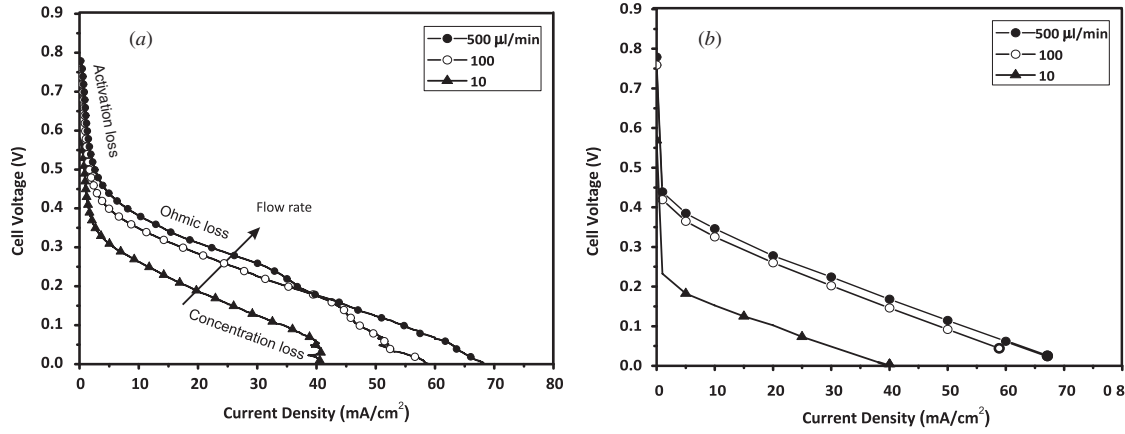


Figure 3. The (a) experimental and (b) simulated polarization curves of the fuel cell running by formic acid. Oxygen is supplied from the atmosphere through a GDE.

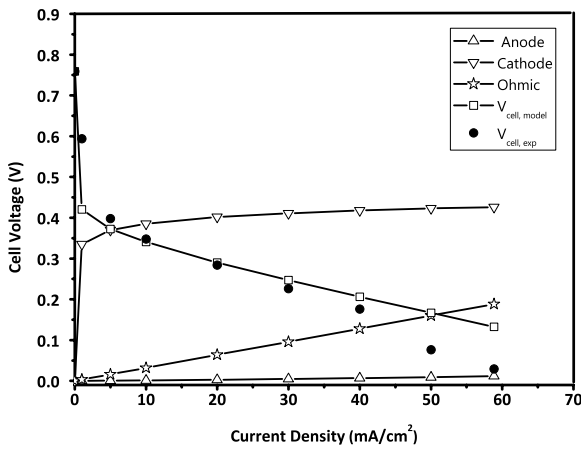


Figure 4. Contribution of different polarization losses.

4.4. Cathode and anode overpotential

In order to solve equation (7), species concentration and activation overpotential must be known for both electrodes. Furthermore, to draw the I – V curve, both voltage and corresponding cell current density must be considered. To

obtain the I – V curve, the cell current is fixed and the corresponding voltage is calculated [28] by taking into account the different polarization losses based on the empirical data of the fabricated cell. It is noteworthy that for any fuel cell, the operating potential can be calculated as the departure from the ideal voltage caused by the various polarizations [29]:

$$E_{\text{cell}} = E^0(T, P) - \eta_{a,a} - |\eta_{a,c}| - \eta_r - \eta_{m,a} - |\eta_{m,c}| - \eta_x, \quad (10)$$

where $E^0(T, P)$ is the theoretical equilibrium open-circuit potential for the cell, calculated from the Nernst equation. $\eta_{a,a}$ and $\eta_{a,c}$ represent the activation overpotentials at the anode and cathode. η_r is the Ohmic loss and occurs because of the resistance to the flow of electrons through the electrode materials and the electric contacts. The mass transfer (concentration) polarizations at the anode and cathode are presented as $\eta_{m,a}$ and $\eta_{m,c}$, respectively. The crossover effect of the fuel/oxidizer through the electrolyte or internal short circuits in the cell can be presented by η_x , which is responsible for the departure of theoretical equilibrium open-circuit potential from the Nernst equilibrium voltage.

Experimental data in figure 3(a) show that there is no sharp drop of the voltage at high current densities for the given geometry and operation conditions. Therefore, to simplify

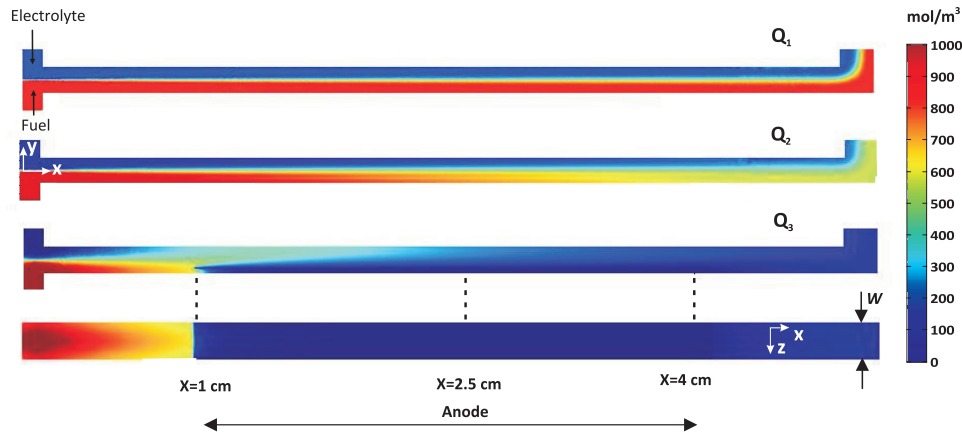


Figure 5. Concentration profiles of formic acid for three flow rates of Q_1 , Q_2 and Q_3 with an inlet concentration of 1000 mol m^{-3} (1 M). The T-shaped cross-section of the channel is located at the x – y plane that cut through the center of the channel ($z = \frac{1}{2}W$) with a width of W .

the modeling, mass transfer overpotential can be neglected. Also the effect of the mixed potential of the cathode and other parasitic losses can be taken into account in the open-circuit potential, which is obtained from experiment. So equation (11) can be considered as a semi-empirical equation and simplified to

$$E_{\text{cell}} = E_{\text{OCV}} - \eta_{a,a} - |\eta_{a,c}| - \eta_r, \quad (11)$$

where E_{OCV} is the experimental open-circuit voltage obtained from the I - V curve at a given flow rate figure 3(a). According to equation (7) the current density is dependent on the concentration of the fuel and the oxidant. So the species concentration can be calculated at a fixed current density with the corresponding activation overpotentials, $\eta_{a,a}$ and $\eta_{a,c}$, while the flow rate is known.

Figure 3(a) shows that the maximum current density (limiting current) is not determined by the mass transfer overpotential, especially for Q_1 and Q_2 . The only exception is the flow rate of $10 \mu\text{l min}^{-1}$ with a short drop observed at the limiting current. So the main overpotential losses are mainly associated with activation and Ohmic losses. The Ohmic losses are mainly attributed to the electrolyte proton conductivity and external resistance of electrodes and connections. Ohmic losses of the cell are calculated by

$$\eta_r = i \cdot (R_{\text{electrolyte}} + R_{\text{external}}), \quad (12)$$

where $R_{\text{electrolyte}}$ is caused by the ionic conductivity of the electrolyte. To determine the ionic conductivity across the channel from the anode to cathode, 0.5 M sulfuric acid is mixed with 1 M of formic acid. The ionic conductivity of 0.5 M sulfuric acid was measured to be 0.2 S cm^{-1} [6].

Based on an anode to cathode spacing of 1.4 mm, a solution resistance of $0.7 \Omega \text{ cm}^2$ is obtained. Cell potential minus activation and electrolyte losses leaves the losses of external resistance R_{external} . A value of 4.9Ω is considered for external resistance, obtained from the electrochemical impedance spectroscopy (EIS) of the cell, including the resistance of wiring and the electrical contacts.

To solve equation (11), E_{OCV} and η_r are obtained from the experimental data, while the anodic and cathodic activation overpotentials, $\eta_{a,a}$ and $\eta_{a,c}$, are obtained from the simulation. In this case, the voltage calculated using equation (11) is called $V_{\text{cell,model}}$.

5. Results and discussion

5.1. Current-voltage polarization curve

The cell potential was calculated using equation (11) at three flow rates of 10, 100 and $500 \mu\text{l min}^{-1}$, figure 3(b). For most data points, there is agreement between experimental and numerical results. At high current densities, especially for $10 \mu\text{l min}^{-1}$, the fluctuations are attributed to the generation of carbon dioxide bubbles over the anode due to electro-oxidation of formic acid, figure 3(a). These bubbles can block the active sites of the anode for a short while but can be dissolved in the stream or washed away by the stream drag force before growing large enough to block the channel. The difference between the experimental and numerical results mainly arises

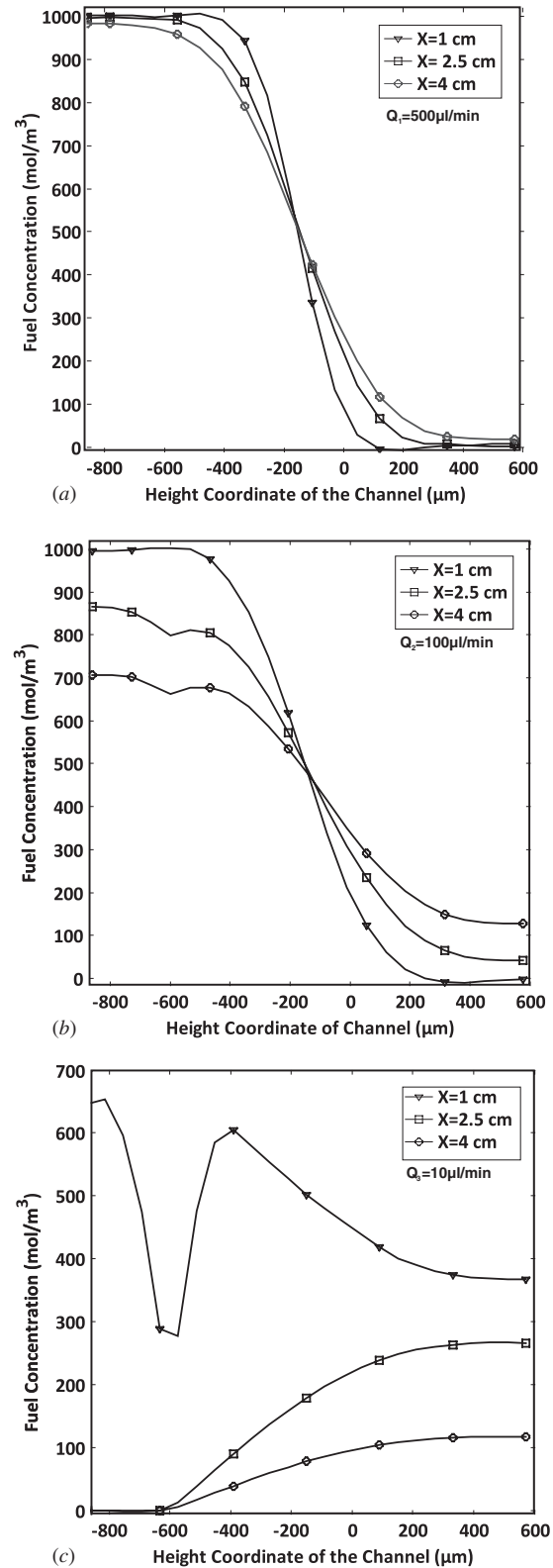


Figure 6. Concentration distribution of formic acid through the channel for three flow rates at three cross sections: (a) $Q_1 = 500 \mu\text{L min}^{-1}$; (b) $Q_2 = 100 \mu\text{L min}^{-1}$ and (c) $Q_3 = 10 \mu\text{L min}^{-1}$. Height coordinate is in the y -direction and the three cross sections are on the centerline of the (y - z) plane ($Z = \frac{1}{2}W$). The porous anode is from -880 to $-600 \mu\text{m}$.

from the concentration losses, which are not taken into account in the simulation.

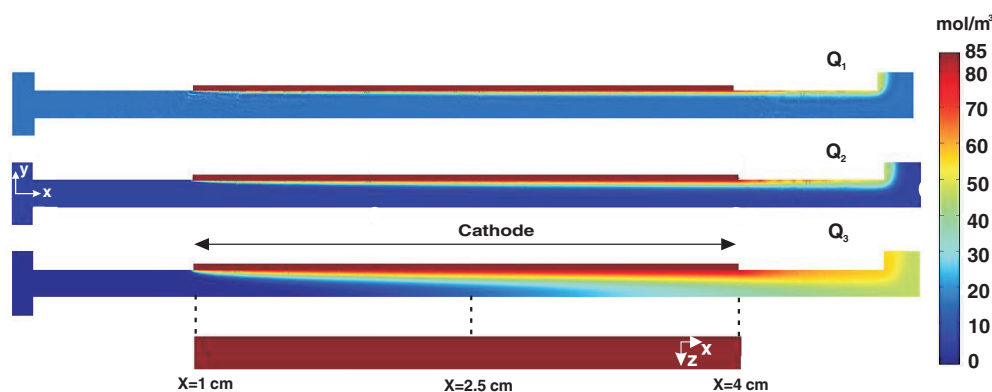


Figure 7. Concentration profiles of oxygen for three flow rates of $Q_1 = 500 \mu\text{L min}^{-1}$, $Q_2 = 100 \mu\text{L min}^{-1}$ and $Q_3 = 10 \mu\text{L min}^{-1}$. The T-shaped cross-section of the channel is located at the x - y plane, which cuts through the center of the channel ($z = \frac{1}{2}W$) with a width of W .

To have a more quantitative visualization of the contribution of the three polarization losses (activation, ohmic and concentration) in decreasing the cell potential, individual losses were plotted in figure 4. Cathodic overpotential due to the sluggish electro-reduction of oxygen has the largest contribution in voltage drop, especially at low current densities. Anodic loss is negligible as compared with the cathodic one. Ohmic loss is linear and increases with growing current density.

5.2. Concentration distribution of formic acid

The typical open-circuit voltage of an air-breathing LFFC with similar fuel and electrolyte is in the range of 0.7–0.9 V [5]. Since the microfluidic fuel cell takes advantage of co-laminar streams, changes in the flow rate affect the transport of reactants and consequently the cell performance.

As figure 5 shows, at the highest flow rate Q_1 , due to the high Peclet number of the stream ($Pe = 850$), the mixing region is limited to a very thin zone at the middle of the channel, while for Q_2 and Q_3 ($Pe = 170$ and 17), diffusion at the liquid–liquid interface is obvious. At Q_3 , the fuel can diffuse across the electrolyte stream and even reach the cathode side.

The catalyst layer over the carbon paper of the anode is inside the channel from $x = 1$ to 4 cm. Fuel consumption over the anode produces a depletion boundary layer. At high flow rates the depleted fuel is replenished by the stream rapidly. Decreasing the feeding flow rate leads to the formation of a zone with low fuel concentration. At the flow rate of Q_3 , the growth of the depletion boundary layer over the anode is obvious.

The fuel cell characteristics shown in figure 3 clearly show three typical regions of activation loss, ohmic loss and concentration loss. Numerical results in figure 5 indicate that the lower diffusive mixing at a high fuel flow rate allows a higher fuel concentration at the anode side leading to the decrease of concentration loss. At medium current densities, all curves are almost parallel indicating the same ohmic resistivity, which is determined by the concentration

of the electrolyte solution, the conductivity of the electrode and electrical interconnects and the spacing between the two electrodes. In the region of concentration loss, the curve of Q_3 in figure 3 shows a higher loss due to the depletion of the fuel as depicted in figure 5. At the high fuel flow rate of $500 \mu\text{L min}^{-1}$, the region of concentration loss is almost non-existent.

A more quantitative illustration of numerical results in figure 5 as concentration distribution in figure 6 obviously reveals that by decreasing the flow rate, the content of formic acid over the cathode increases. Decreasing the flow rate increases the residence time of the fuel and the electrolyte in the channel and enhances diffusive mixing at the interface [11]. Figure 6(a) shows that fuel concentration over cathode at the end of the cathode ($x = 4$ cm) is almost zero. The underlying reason is that the residence time of flow in the channel (~ 10 s) is so short compared to Q_2 and Q_3 (~ 50 and ~ 500 s). The corresponding values of the fuel concentration of Q_2 and Q_3 are 120 and 260 mol m^{-3} , respectively. The fuel crossover is significant at lower flow rates and has two consequences. First, the concentration of the fuel in the anolyte stream decreases and has an impact on decreasing the current density. Second, the electro-oxidation of formic acid over the cathode can result in a mixed potential and reduces the open-circuit potential. The numerical model shows that the main reason for the drop of the open-circuit potential from 0.78 V with Q_1 to 0.58 V with Q_3 is fuel crossover and the mixed potential at the cathode.

5.3. Concentration distribution of oxygen

The objective of using a GDE as an air-breathing cathode is to provide higher oxygen content at the cathode. In the numerical simulation, the cathode catalyst layer is considered as a boundary at the inner side of the channel where the electro-reduction of oxygen takes place, figure 1.

As figure 7 shows, oxygen can diffuse through the GDE to reach the catalyst layer. Although the oxygen cations are formed over the cathode catalyst layer and supposed to be fixed, oxygen can pass through the GDE and reach the liquid and then diffuse into the aqueous streams in the channel. It

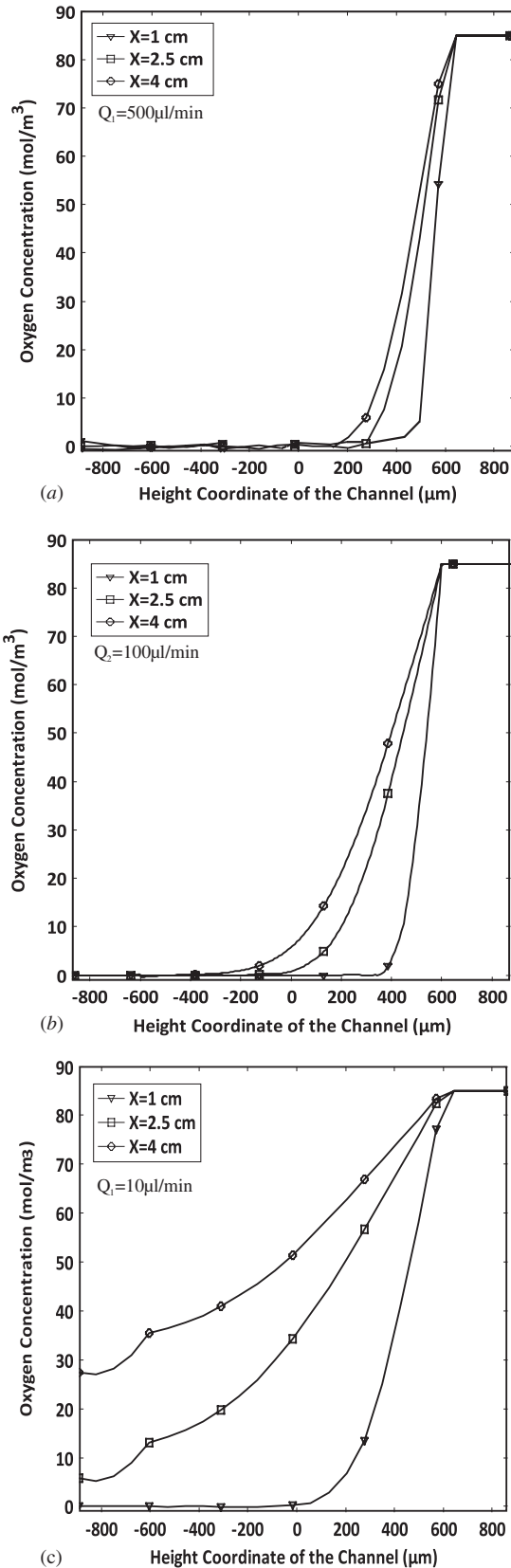


Figure 8. Concentration distribution of oxygen through the channel at three cross sections: (a) $Q_1 = 500 \mu\text{L min}^{-1}$; (b) $Q_2 = 100 \mu\text{L min}^{-1}$ and (c) $Q_3 = 10 \mu\text{L min}^{-1}$. The height coordinate is in the y-direction and the three cross sections are on the centerline of (y-z) plane ($Z = \frac{1}{2}W$). The porous anode is from -880 to $-600 \mu\text{m}$.

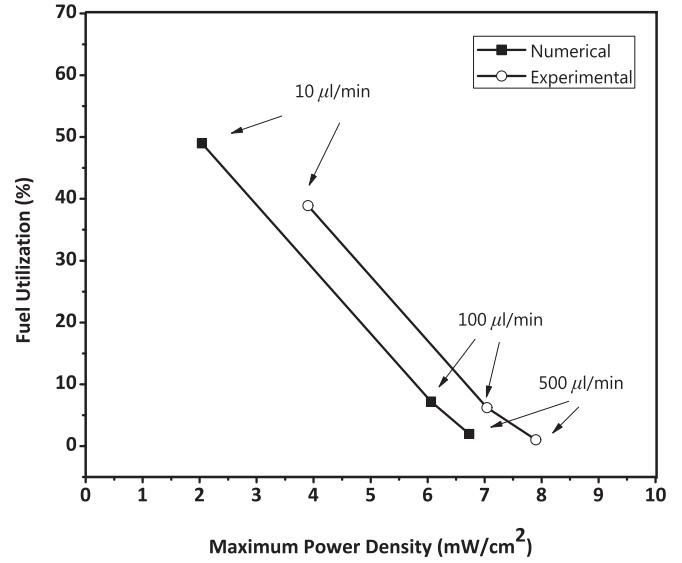


Figure 9. The experimental and simulated fuel utilization versus maximum power density.

is evident that the oxygen concentration through the GDE is almost constant.

Furthermore, figure 8 shows that unlike a LFFC with oxidant stream, the oxygen concentration in the vicinity of the cathode active area is almost constant. For all three flow rates, a sharp drop of the oxygen concentration of the electrolyte rather than that of the electrode is observable. This sharp drop is attributed to the difference in the higher diffusion coefficient of oxygen in porous media ($D_{\text{O}_2(\text{GDE})} = \frac{\varepsilon}{\tau} \times 2 \times 10^{-5} \text{ m}^2 \text{ s}^{-1}$) and in water ($2 \times 10^{-9} \text{ m}^2 \text{ s}^{-1}$).

The flow rate of the laminar streams inside the channel can affect the oxygen transport through the channel. At the higher flow rates of Q_1 and Q_2 , the transported oxygen to the channel cannot diffuse to the anolyte stream and is washed away with the electrolyte stream. At a very low flow rate (Q_3), oxygen has more residence time inside the channel to diffuse to the anolyte stream. The oxygen content over the catalyst layer of the anode at the distance of $x = 4 \text{ cm}$ (the end of the anode) is around 35 mol m^{-3} . Diffusion of oxygen across the channel may result in oxygen crossover. The oxygen crossover to the anode may facilitate electro-reduction of oxygen and cause mixed potential resulting in a lower open-circuit potential. Since the voltage of the anode is very low compared to the cathode potential, the effect of oxygen reduction on cell potential is minor.

5.4. Fuel utilization and power density

Figure 9 shows the effect of raising the flow rate from 10 to $500 \mu\text{L min}^{-1}$ on fuel utilization versus maximum power density under different flow rate conditions. The improvement of power density at higher flow rates can be associated with (a) the higher voltage generated due to the lower mixed potential at the cathode and (b) the higher rate of electrochemical reaction to generate current because of the higher availability of reactants in the vicinity of the catalytic active sites. According to equation (7), current generation over

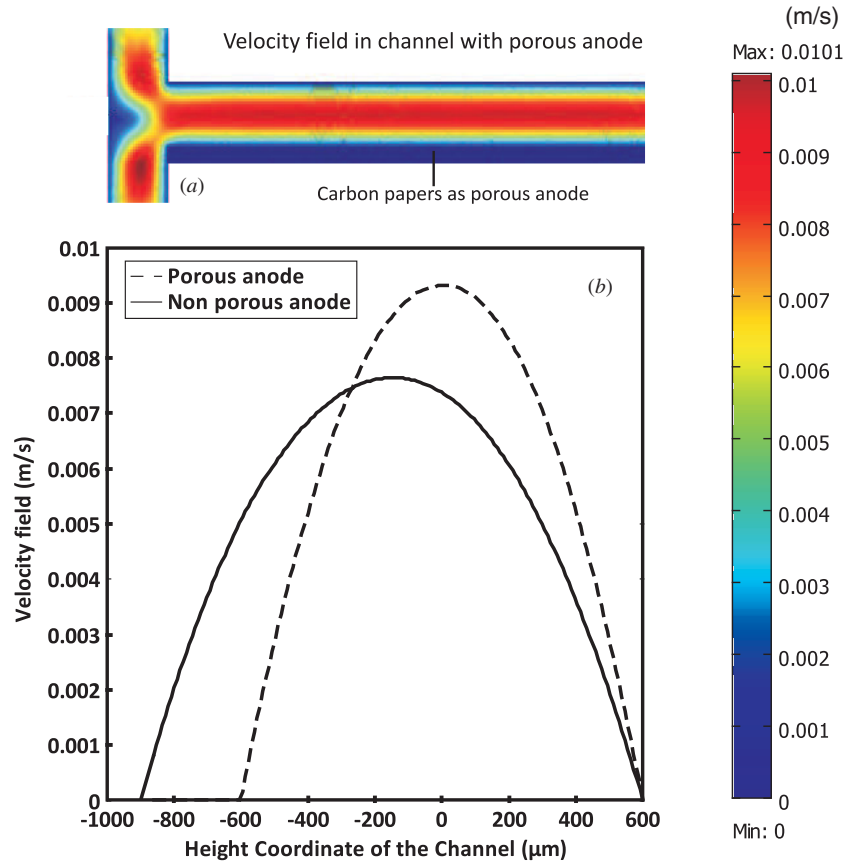


Figure 10. Flow field simulation: (a) simulated velocity field in the channel with the porous anode and (b) velocity profile across the channel for the porous and non-porous anodes at a flow rate of $500 \mu\text{l min}^{-1}$.

the anode is highly dependent on the concentration of formic acid. Beside the low fuel concentration over the anode, the low open-circuit potential is another reason for the low power density of Q_3 .

Fuel utilization is determined as [31]:

$$\varepsilon_{\text{fuel}} = \frac{I}{nFQ_{\text{fuel}}}, \quad (13)$$

where I is the current generated by the fuel cell, Q_{fuel} is the fuel rate supplied to the cell in mol s^{-1} and n is the number of electrons transferred for every mol of the fuel. In the case of formic acid, $n = 2$, $F = 96485 \text{ C mol}^{-1}$ is the Faraday constant. Figure 9 clearly shows that a higher fuel flow rate leads to a high power density but a low fuel utilization.

At the flow rates of 10, 100 and $500 \mu\text{l min}^{-1}$, the experimental fuel utilizations of the cell at maximum experimental power density are 38.9, 6.23 and 1.03%, respectively. At the same flow rates, the numerical fuel utilizations of the cell at the corresponding power densities are 49.6, 7.21 and 1.95%, as depicted in figure 9. It is obvious that there is a good trend between experimental and numerical results, but a quantitative difference is observed for the flow rate of $10 \mu\text{l min}^{-1}$. Concentration (mass transport) loss can decrease the cell potential at high current densities and especially for $10 \mu\text{l min}^{-1}$. Since the simulation does not include the impact of concentration losses on the cell potential, error in calculating the cell potential could be introduced.

Moreover, experimental uncertainties can be another source for this difference.

As figures 5 and 6 illustrate, for the flow rates of 100 and $500 \mu\text{l min}^{-1}$, the fuel concentration over the anode is still high enough to produce more current, but only a part of the stream in the vicinity of the electrode is consumed. It seems that the core part of the flow including a high concentration of the fuel just passes through the channel without any contribution in producing current. The high fuel utilization of the cell at $10 \mu\text{l min}^{-1}$ is contributed by the longer residential time in the channel leading to more fuel consumption.

As the flow rate of the laminar streams decreases almost two orders of magnitude from 500 to $10 \mu\text{l min}^{-1}$, the corresponding maximum power density only drops from approximately 7.9 to 3.9 mW cm^{-2} . In this case, fuel utilization increases from 1.03 to 38.9%. Unlike the conventional LFFCs, whose performances usually drop dramatically with decreasing fuel and oxidant flow rates [2, 30], the power output of a LFFC with an air-breathing cathode is less sensitive to the flow rate compared to conventional LFFCs. An air-breathing LFFC with optimized flow architecture operating in very low flow rates seems to be a suitable power source for practical operations.

The anode is made of porous carbon paper, which can present more active area rather than a non-porous and planar anode. The implementation of carbon paper in the channel is supposed to replenish the depletion boundary layer. However,

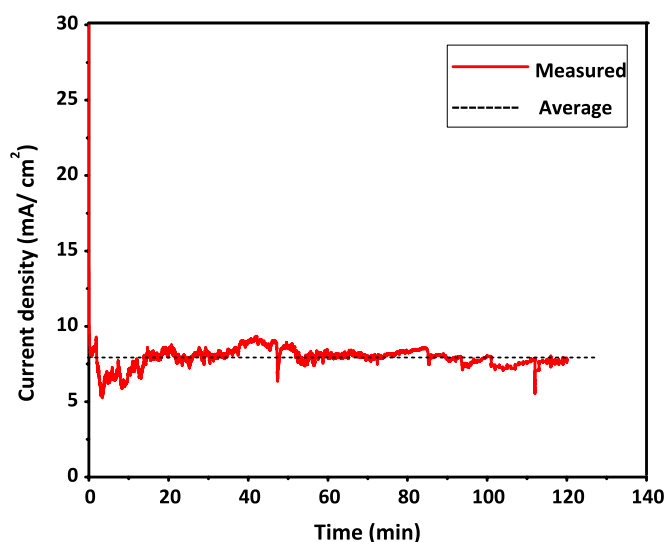


Figure 11. Steady-state chronoamperometric measurement at 0.25 V cell potential and $100 \mu\text{L min}^{-1}$ flow rate.

the numerical simulation of the flow field within the channel with the porous anode reveals that the velocity of liquid in porous media is almost zero, figure 10(a). In other words, there is no effective advective mass transport through the porous anode to provide fresh reactants to the active sites.

Using the concept of the ‘flow-through porous electrode’ [30] to design the anode can promote the replenishment of the depletion layer by enhanced advective transport to develop the fuel utilization. Also, a new configuration of the channel, which can facilitate the mass transfer from the core part of the fuel stream to the active area of the anode, without disturbing the interface, can be considered as a strategy to develop the fuel utilization at high flow rates.

Figure 11 depicts the long-term stability of the current generated by the air-breathing fuel cell evaluated by a potentiostatic test at 0.25 V cell voltage and $100 \mu\text{L min}^{-1}$ flow rate. After a brief transient period, the cell current density is stable over the 2 h of experiment with an average value of 7.92 mA cm^{-2} . The fluctuations could be caused by CO_2 bubbles occupying active sites in the porous anode. Since CO_2 bubbles can be dissolved in the aqueous media, the occupied micro pores with carbon dioxide in the electrode can be refilled with the fuel again. This phenomenon of CO_2 generation and replenishment could cause fluctuations in the generated current.

6. Conclusions

This paper reports on the fabrication, characterization and simulation of an air-breathing LFFC running on formic acid with an integrated porous planar electrode as an anode inside the channel. The fuel cell was fabricated using laser micromachining and characterized at three different flow rates. The experimental results demonstrate that at high flow rates the open-circuit voltage is higher, but low fuel utilization is achieved imposing some requirements for fuel recirculation for real applications. The high rate of fuel utilization at

high cell potentials is desirable to achieve high overall energy conversion efficiency. As a general design consideration, a compromise between high fuel utilization rate and high mass-limitation loss needs to be met. Exploiting a flow-through porous anode can provide advective mass transport to replenish the depletion layer over the anode to develop fuel utilization and current density. Operation in low flow rates results in high fuel utilization. Optimizations of air-breathing LFFC for operation in low flow rates to achieve high fuel utilization can eliminate the requirements for fuel utilization. In this case, an air-breathing LFFC has more possibilities as a power source for micro-power applications.

Acknowledgment

SAMS would like to acknowledge the scholarship from A*STAR (Agency for Science Technology and Research) to pursue postgraduate studies.

References

- [1] Ferrigno R, Stroock A D, Clark T D, Mayer M and Whitesides G M 2002 Membraneless vanadium redox fuel cell using laminar flow *J. Am. Chem. Soc.* **124** 12930–1
- [2] Li A, Chan S H and Nguyen N T 2007 A laser-micromachined polymeric membraneless fuel cell *J. Micromech. Microeng.* **17** 1107–13
- [3] Kjeang E, Brolo A G, Harrington D A, Djilali N and Sinton D 2006 Hydrogen peroxide as an oxidant for microfluidic fuel cells *J. Electrochem. Soc.* **154** B1220–6
- [4] Kjeang E, McKechnie J, Sinton D and Djilali N 2007 Planar and three-dimensional microfluidic fuel cell architectures based on graphite rod electrodes *J. Power Sources* **168** 379–90
- [5] Jayashree R S, Gancs L, Chohan E R, Primak A, Natarajan D, Markoski L J and Kenis P J A 2005 Air-breathing laminar flow-based microfluidic fuel cell *J. Am. Chem. Soc.* **127** 16758–9
- [6] Jayashree R S, Egas D, Spendelow J S, Natarajan D, Markoski L J and Kenis P J A 2006 Air-breathing laminar flow-based direct methanol fuel cell with alkaline electrolyte *Electrochem. Solid-State Lett.* **9** A252–6
- [7] Whipple D T, Jayashree R S, Egas D, Alonso-Vante N and Kenis P J A 2009 Ruthenium cluster-like chalcogenide as a methanol tolerant cathode catalyst in air-breathing laminar flow fuel cells *Electrochim. Acta* **54** 4384–8
- [8] Hollinger A S, Maloney R J, Jayashree R S, Natarajan D, Markoski L J and Kenis P J A 2010 Nanoporous separator and low fuel concentration to minimize crossover in direct methanol laminar flow fuel cells *J. Power Sources* **195** 3523–8
- [9] Tominaka S, Ohta S, Obata H, Momma T and Osaka T 2008 On-chip fuel cell: micro direct methanol fuel cell of an air-breathing, membraneless, and monolithic design *J. Am. Chem. Soc.* **130** 10456–7
- [10] Jayashree R S, Yoon S K, Brushett F R, Lopez-Montesinos P O, Natarajan D, Markoski L J and Kenis P J A 2010 On the performance of membraneless laminar flow-based fuel cells *J. Power Sources* **195** 3569–78
- [11] Bazylak A, Sinton D and Djilali N 2005 Improved fuel utilization in microfluidic fuel cells: a computational study *J. Power Sources* **143** 57–66
- [12] Chen W and Chen F 2006 Theoretical approaches to studying the single and simultaneous reactions in laminar flow-based membraneless fuel cells *J. Power Sources* **162** 1137–46

- [13] Chang M H, Chen F and Fang N S 2006 Analysis of membraneless fuel cell using laminar flow in a Y-shaped microchannel *J. Power Sources* **159** 810–6
- [14] Chen F, Chang M H and Hsu C W 2007 Analysis of membraneless microfuel cell using decomposition of hydrogen peroxide in a Y-shaped microchannel *Electrochim. Acta* **52** 7270–7
- [15] Lee J, Lim K G, Palmore G, Tayhas R and Tripathi A 2007 Optimization of microfluidic fuel cells using transport principles *Anal. Chem.* **79** 7301–7
- [16] Xu J B, Zhao T S and Liang Z X 2008 Carbon supported platinum–gold alloy catalyst for direct formic acid fuel cells *J. Power Sources* **185** 857–61
- [17] Uhm S, Lee H J and Lee J 2009 Understanding underlying processes in formic acid fuel cells *Phys. Chem. Chem. Phys.* **11** 9326–36
- [18] Park G G, Sohn Y J, Yang T H, Yoon Y G, Lee W Y and Kim C S 2004 Effect of PTFE contents in the gas diffusion media on the performance of PEMFC *J. Power Sources* **131** 182–7
- [19] Song C and Zhang J 2008 Electrocatalytic oxygen reduction reaction *PEM Fuel Cell Electrocatalysts and Catalyst Layers: Fundamentals and Applications* ed J Zhang (Berlin: Springer) pp 89–129
- [20] Yeom J, Jayashree R S, Rastogi C, Shannon M A and Kenis P J A 2006 Passive direct formic acid microfabricated fuel cells *J. Power Sources* **160** 1058–64
- [21] Rice C, Ha S, Masel R I, Waszczuk P, Wieckowski A and Barnard T 2002 Direct formic acid fuel cells *J. Power Sources* **111** 83–9
- [22] Nield D A and Bejan A 2006 *Convection in Porous Media* (Berlin: Springer)
- [23] O'Hayre R, Fabian T, Litster S, Prinz F B and Santiago J G 2007 Engineering model of a passive planar air breathing fuel cell cathode *J. Power Sources* **167** 118–29
- [24] Chen R and Zhao T S 2005 Mathematical modeling of a passive-feed DMFC with heat transfer effect *J. Power Sources* **152** 122–30
- [25] Chen F, Chang M H and Lin M K 2008 Analysis of membraneless formic acid microfuel cell using a planar microchannel *Electrochim. Acta* **52** 2506–14
- [26] Zhang L J, Wang Z Y and Xia D G 2006 Bimetallic PtPb for formic acid electro-oxidation *J. Alloys Compounds* **426** 268–71
- [27] Feser J P, Prasad A K and Advani S G 2006 Experimental characterization of in-plane permeability of gas diffusion layers *J. Power Sources* **162** 1226–31
- [28] Chan S H, Khor K A and Xia Z T 2001 A complete polarization model of a solid oxide fuel cell and its sensitivity to the change of cell component thickness *J. Power Sources* **93** 130–40
- [29] Mench M M 2008 *Fuel Cell Engines* (New York: Wiley)
- [30] Kjeang E, Michel R, Harrington D A, Djilali N and Sinton D 2008 A microfluidic fuel cell with flow-through porous electrodes *J. Am. Chem. Soc.* **130** 4000–6
- [31] O'Hayre R P, Cha S W, Colella W and Prinz F 2006 *Fuel Cell Fundamentals* (New York: Wiley)